nature sustainability

Article

https://doi.org/10.1038/s41893-026-01967-9

Small-molecule-bound biopolymer networks for sustainable multifunctional composites

Received: 15 February 2026

Accepted: 18 September 2026

Published online: 16 October 2026

Check for updates

Alitenai Tunuhe[1,2], Ze Zheng[1], Ke Zhu[1], Yiquan Zhao[1], Fuying Ma[1], Yadi Gu[3], Junqi Sha[2], Hongbo Yu[1] ✉, Yaxian Zhou[2] ✉ & Shangxian Xie[1,2] ✉

Multicomponent biopolymer networks are promising platforms for developing sustainable materials. However, weak coupling across mismatched heterointerfaces of different biomaterials limits structural coherence, load transfer and functional integration. Here we establish a natural small-molecule-mediated non-covalent heterointerfacial reorganization strategy and validate it using a collagen–*Ganoderma lucidum* mycelium–plant-derived anthocyanin (CMpA) model system. By combining molecular simulations, interfacial spectroscopy, mesoscale structural analysis and mechanical modelling, we resolve a cross-scale pathway in which anthocyanin-associated non-covalent contacts at local heterointerfaces are translated into pore-wall consolidation, lamellar orientational coherence and continuous load transfer. This cross-scale structural integration yielded CMpA films with a tensile strength of 63.55 MPa, along with UV-shielding, antioxidant and antibacterial properties, reduced oxygen and water-vapour transmission, and pH-responsive freshness indication, making them promising candidates for active and intelligent packaging. More broadly, the work links small-molecule-mediated local interfacial chemistry with mesoscale anisotropic network formation and macroscopic functional integration, offering a design principle for sustainable biopolymer materials that require both mechanical coherence and multifunctionality.

The synergy between rigid and compliant phases enables composites to sustain loads while dissipating energy[1,2]. Yet, reliable macroscopic performance depends not simply on the intrinsic strength of individual constituents, but on the establishment of multiscale structural order[2,3]. Such order creates percolating load-transfer pathways and suppresses stress localization[3,4]. Although field-assisted assembly can induce disorder-to-order transitions and programmable anisotropy[5], achieving comparable anisotropy in sustainable biomimetic composites remains challenging[3,6]. In particular, structural coherence is often restricted to building blocks with inherent assembly motifs[7,8]. Developing chemically simple ambient-condition routes to organize heterogeneous biomass into high-performance and mechanistically interpretable materials therefore remains an important challenge for sustainable materials design[8].

This challenge is particularly evident in multicomponent biopolymer networks. Bioactive macromolecules, which combine molecular

[1]Department of Biotechnology, College of Life Science and Technology, Huazhong University of Science and Technology, Wuhan, Hubei, China. [2]Guangxi Shenguan Collagen Technology Research Institute, Guangxi Shenguan Collagen Biological Group Company Limited, Wuzhou, Guangxi, China. [3]Halıcıoğlu Data Science Institute, University of California San Diego, La Jolla, CA, USA. ✉e-mail: yuhongbo@hust.edu.cn; xiansheng@vip.163.com; shangxian_xie@hust.edu.cn

https://doi.org/10.1038/s41893-026-01967-9

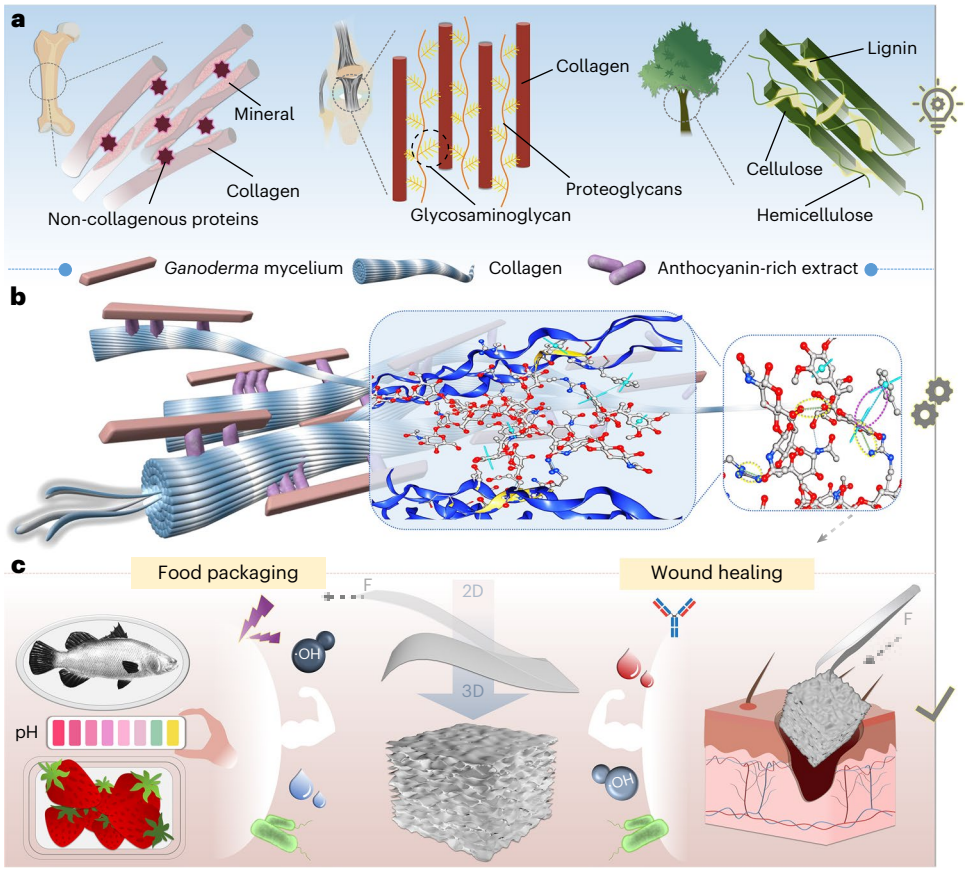


Fig. 1 | Nature-inspired interfacial mediation and small-molecule-mediated reorganization of heterogeneous biopolymer networks. a, Representative biological archetypes showing how localized interfacial mediators regulate heterogeneous macromolecular organization in natural structural materials, including mineral–collagen coupling in bone, proteoglycan-regulated collagen fibril spacing in ligaments and lignin–polysaccharide association in plant cell walls. **b**, Design rationale of plant-derived anthocyanin-mediated collagen–mycelium composites (CMpA). Mycelium-derived fibrous reinforcing domains (M) and compliant collagen scaffolds (C) are integrated through plant-derived anthocyanin (pA), which acts as a non-covalent interfacial mediator at C–M heterointerfaces. Multivalent hydrogen bonding and aromatic-associated interactions are proposed to promote pore-wall consolidation, improved C–M interfacial continuity and mesoscale lamellar orientational coherence. In the molecular representations, collagen is shown as blue ribbons, whereas the remaining molecular components are shown in stick representation; carbon, oxygen and nitrogen atoms are shown in grey, red and blue, respectively. **c**, Functional translation of the CMpA architecture. The reorganized ternary network can be processed into active/intelligent food-packaging films with mechanical integrity, barrier properties, antibacterial/antioxidant activity and pH-responsive freshness indication, and further extended into porous aerogel formats for proof-of-concept haemostatic application.

recognition, self-assembly and intrinsic biological functions, provide a promising sustainable platform for high-performance composites[9–11]. Nevertheless, translating structural-ordering concepts to complex biopolymer networks remains formidable[12,13]. Multivalent weak interactions among heterologous biopolymers often lead to non-ideal mixing and mesoscale segregation, where compositional gradients and interfacial boundaries disrupt cross-network coupling and weaken percolated connectivity[8,12,13]. Concurrently, stress-structure coupling during processing remodels nascent fibrillar motifs and redistributes local stresses, diminishing persistent mesoscale structural coherence[13,14]. Thus, the key limitation in heterogeneous biopolymer assemblies is not simply insufficient constituent strength, but the lack of controlled interfacial coupling and continuity.

Natural structural materials provide design inspirations for how localized interfacial regulation can coordinate heterogeneous macromolecular networks into mechanically coherent architectures (Fig. 1a). In bone, non-collagenous proteins direct mineral nucleation, ensuring ordered hydroxyapatite deposition within collagen scaffolds[15,16]. Plant cell walls achieve analogous control when lignin associates with polysaccharides, contributing to framework stiffening and hierarchical organization[17–19]. Likewise, proteoglycans in ligaments modulate fibrillogenesis by occupying discrete sites on collagen fibrils, while their glycosaminoglycan chains generate steric and electrostatic repulsion that maintains uniform fibril spacing, prevents random entanglement, and helps maintain tissue-level organization[20,21]. Collectively, these examples highlight a design principle directly relevant to artificial bio-based materials: localized interfacial cues can regulate the organization of macromolecular networks by acting at heterogeneous boundaries[22]. This principle motivates the use of bio-derived small molecules as artificial non-covalent interfacial mediators for selected heterogeneous biopolymer networks. However, artificial rigid-compliant systems remain difficult to control because hydration-driven self-association in protein networks[23–25], and wetting-induced discontinuities in chitin/glucan-rich mycelial scaffolds restrict entanglement and load transfer[26,27]. This underscores the need for precise interfacial control to reconcile intrinsic incompatibilities and guide stochastic mixtures towards hierarchically ordered, mechanically integrated biocomposites[27,28].

In this study, we report an alternative strategy using a small molecule to achieve non-covalent heterointerfacial reorganization between two distinct biopolymers under mild conditions without relying on covalent crosslinking or harsh chemical modification (Fig. 1b). As a representative model system, *Ganoderma lucidum* mycelium (M) and collagen (C) were selected as structurally and mechanically contrasting

bio-derived components. In this model, the relevant heterointerface is defined as the contact region between collagen-rich domains and mycelium-derived cell-wall/fibrillar domains[24,25,29]. To regulate this intrinsically mismatched interface, plant-derived anthocyanins (pA) were introduced as bioactive non-covalent interfacial mediators. Their polyphenolic hydroxyl groups and aromatic motifs provide multiple non-covalent interaction sites, while their antioxidant and pH-responsive properties, together with the antibacterial activity evaluated in this work, make them relevant to active and intelligent packaging (Fig. 1c)[30,31]. We hypothesized that pA associates with both collagen-rich and mycelium-derived domains through multivalent hydrogen bonding, polar association and aromatic/dispersion interactions, thereby reorganizing discontinuous C–M contact regions into a more continuous ternary network rather than acting as a conventional bulk crosslinker or simple additive.

To test this hypothesis, we examined the CMpA system across molecular, structural and mechanical length scales. Interfacial characterization was used to probe anthocyanin-mediated association at the collagen–mycelium boundary, while microscopy and scattering analyses evaluated pore-wall continuity and lamellar orientational coherence. Multiscale modelling further connected local interfacial interactions with load sharing and damage localization in the reorganized network. Together, this framework allowed us to examine whether plant-derived small molecules can act as interfacial mediators to reorganize heterogeneous biopolymer assemblies into mechanically integrated and functionally active architectures. More broadly, this interface-directed strategy provides a design route for selected small-molecule-mediated biopolymer heterointerfaces, with potential relevance to interfacial compatibility and mesoscale ordering challenges in multicomponent bio-based materials.

Results

pA-mediated interfacial reorganization and mesoscale order

To construct an active interpenetrating composite with a biomimetic lamellar architecture[3], we employed plant-derived anthocyanin (pA) as a non-covalent small-molecule interfacial mediator to regulate collagen–mycelium (C–M) heterointerfacial coupling within a C–M matrix[32,33]. Environmental scanning electron microscopy (ESEM, Fig. 2a) revealed a pronounced morphology change associated with pA-mediated interfacial regulation. The binary CM composite exhibited a disordered, densely entangled network with local phase heterogeneity and discontinuous pore-wall features. In contrast, the ternary collagen–mycelium–plant-derived anthocyanin (CMpA) composite displayed a more continuous lamellar pore-wall architecture, aligned channel-like features and improved C–M interfacial continuity after pA incorporation. Confocal laser scanning microscopy (CLSM, Fig. 2b and Supplementary Fig. 1) further showed enhanced microscale interpenetration and spatial coordination between collagen fibres and mycelium in CMpA. These observations indicate that pA promotes a transition from an irregular/discontinuous C–M network towards a more-coherent lamellar pore-wall architecture[33].

We also observed component-specific structural responses to pA. In the CpA (collagen–plant-derived anthocyanin) composite, pA reinforced the lamellar porosity with densified pore walls, whereas in the MpA, it refined the dense lamellae into a more delicate porous network (Fig. 2d). This dual regulation drove a mycelium-dependent architectural evolution within the ternary system, from fragmented reorganized regions in $CMpA_2$ to a more continuous mesoscale lamellar framework in $CMpA_5$ (Fig. 2d). This progressive evolution enhanced the integrity of the interpenetrating network and improved the spatial coordination between collagen-rich and mycelium-derived domains. Quantitative orientation analysis with the orientation entropy (*H*) and Herman's orientation factor (*S*) from ESEM images further supported this trend (Fig. 2e,f)[34,35]. The increasing mycelium (M) content within the pA-containing ternary network led to a monotonic reduction in *H* and a simultaneous increase in *S*. These changes indicated progressively enhanced mesoscale orientational coherence, consistent with lamellar densification and reduced porosity relative to CM (Fig. 2k, and Supplementary Fig. 2 and Note 1.1).

The lamellar features observed by microscopy were further examined by small-angle X-ray scattering (SAXS) to resolve their mesoscale structural character. In the two-dimensional (2D) SAXS patterns (Fig. 2g), CMpA displayed a more pronounced elliptical scattering profile and a narrower azimuthal intensity distribution than the nearly isotropic M network and the weakly oriented CM composite, indicating enhanced mesoscale anisotropy within the C–M network. The absence of sharp periodic peaks in the $I(q)$ profiles, where I is the scattering intensity and q is the magnitude of the scattering vector, indicated that no new crystalline domains or molecular-scale periodic ordering were formed. Instead, the strengthened broad correlation feature in $q^2I(q)$ was consistent with improved pore-wall/phase-domain correlation and mesoscale network coherence (Supplementary Fig. 3c,d and Note 1.2).

The emergence of mesoscale coherence was accompanied by changes in interfacial association and local chemical environments (Fig. 2h,i). Surface plasmon resonance (SPR) showed that the M–pA complex retained a comparable apparent affinity to collagen but dissociated more slowly, supporting a more persistent interfacial association rather than an isolated high-affinity pA–collagen interaction. This behaviour suggested that pA increased the persistence of C–M interfacial contacts, rather than functioning as an isolated high-affinity collagen-binding ligand (Supplementary Fig. 3a and Note 1.3). Circular dichroism (CD) spectra indicated that pA alters the local chiral and intermolecular environment of collagen while retaining triple-helix-related features, arguing against complete denaturation. The CD response was therefore interpreted as indicating that pA perturbed the collagen-related environment without evidencing de novo fibrillogenesis (Supplementary Fig. 3b and Note 1.3). In parallel, X-ray photoelectron spectroscopy (XPS) revealed a redistribution of C 1 s, N 1 s and O 1 s chemical states in CMpA, consistent with pA-associated changes in the local chemical environment rather than the formation of a new covalent bonding motif. When considered together with the CpA and MpA controls, the XPS results support component-dependent pA association with collagen-rich and mycelium-derived domains (Fig. 2j, and Supplementary Fig. 4 and Note 1.4). These results collectively support pA-associated non-covalent interfacial association and local chemical-environment reorganization at the C–M heterointerface. Complementary spectroscopic and thermal analyses further support local interfacial reorganization, while viability assays confirm that mycelia remain viable throughout fabrication (Fig. 2c,l,n, and Supplementary Notes 1.5 and 1.6)[36–39]. Processing-sequence and mediator controls further indicate that pA acts preferentially at pre-existing C–M heterointerfaces and that this response is chemically selective (Supplementary Note 1.7 and Fig. 7).

Taken together, these results indicate that pA does not simply act as an additive within the C–M mixture. Rather, pA is associated with local non-covalent redistribution of chemical environments and contact persistence at heterogeneous C–M boundaries, as supported by XPS, SPR, CD and complementary spectroscopic analyses. This local interfacial regulation is translated into pore-wall consolidation, improved network continuity and enhanced mesoscale lamellar orientational coherence, as resolved by microscopy, orientation analysis and SAXS. In this framework, the CMpA architecture is interpreted as an interface-reorganized ternary network that provides the structural basis for the reinforced mechanical response described below.

Cross-scale reinforcement from interface to network

We verified that the resulting interpenetrating network was not merely a structural arrangement, but a functional framework for efficient stress transfer and energy dissipation. To understand the link between the interface and bulk material, we correlated

https://doi.org/10.1038/s41893-026-01967-9

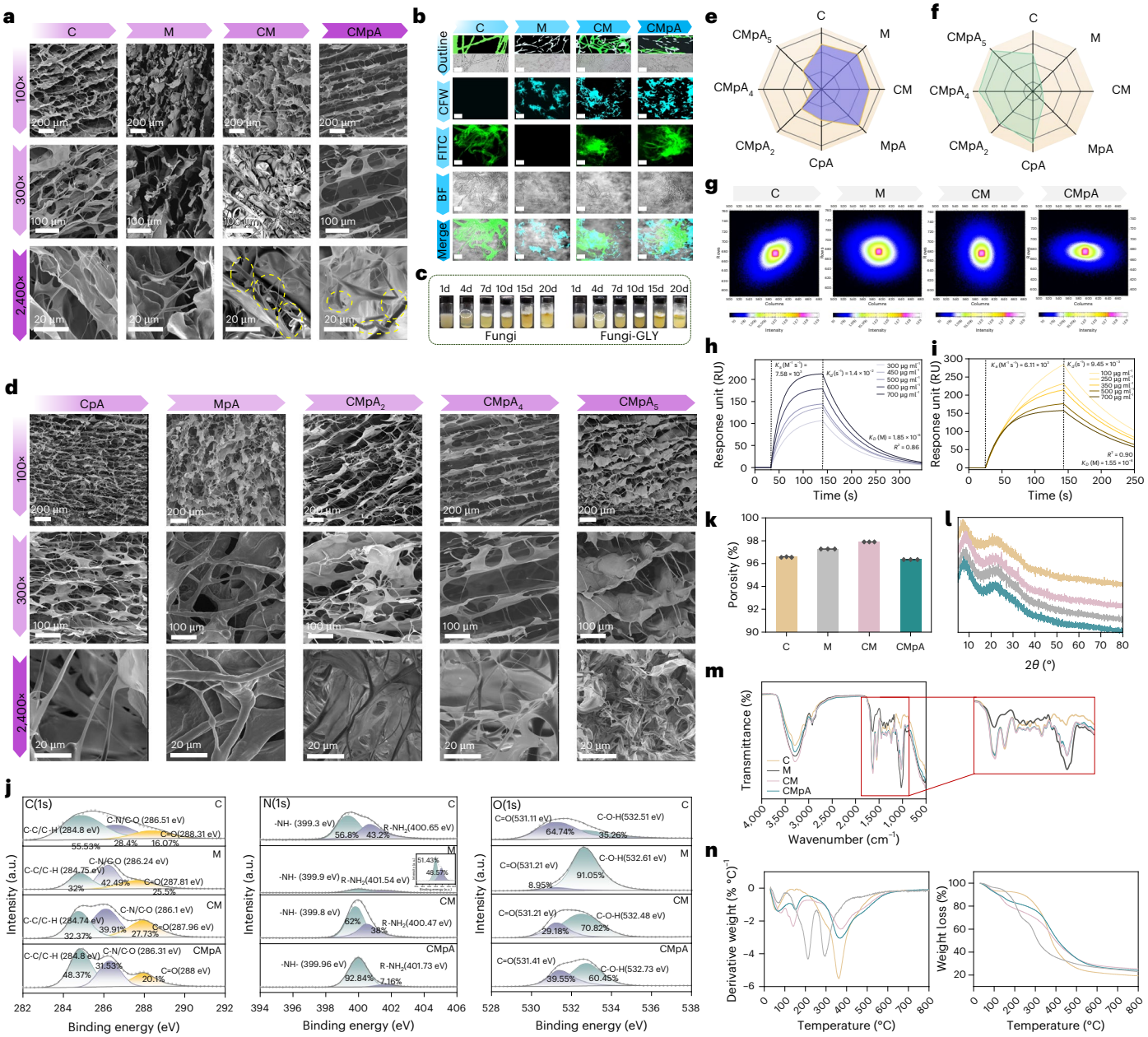


Fig. 2 | pA-mediated hierarchical reorganization of the CMpA network into a lamellar pore-wall architecture with enhanced mesoscale orientational coherence. a, ESEM micrographs of C, M, CM and CMpA, showing the transition from a disordered entangled network to a lamellar porous architecture after pA incorporation. Yellow dashed circles indicate representative regions of collagen–mycelium interpenetration and entanglement. Scale bars, 200 μm (100×), 100 μm (300×) and 20 μm (2,400×). **b**, Confocal fluorescence images showing enhanced microscale interpenetration and spatial coordination in CMpA. M was stained with CFW in blue and C was labelled with FITC in green. Scale bars, 20 μm. **c**, Regenerative growth of mycelium with and without glycerin, confirming preserved biological activity after assembly. White dashed circles indicate representative regions of visible mycelial growth. **d**, ESEM images of CpA, MpA, $CMpA_2$, $CMpA_4$ and $CMpA_5$, showing progressive tuning of mesoscale lamellar ordering with increasing mycelium content. Scale bars, 200 μm (100×), 100 μm (300×) and 20 μm (2,400×). **e**,**f**, Orientation radar plots and quantitative orientation metrics, including orientation entropy (*H*) (**e**) and Herman's orientation factor (*S*) (**f**), showing pA-driven transition from random orientation to enhanced mesoscale orientational coherence. **g**, 2D SAXS patterns of C, M, CM and CMpA, showing enhanced anisotropic scattering and mesoscale organization in CMpA. **h**,**i**, SPR response curves at increasing analyte concentrations, showing concentration-dependent binding and dissociation behaviours consistent with C–M–pA interfacial affinity. **j**, Deconvoluted XPS C 1 s, N 1 s and O 1 s spectra, showing redistributed carbonyl, hydroxyl, amino and C–O/C–N chemical environments in CMpA. **k**, Porosity statistics showing densification associated with thickened lamellar walls. Data are presented as mean ± s.d. ($n = 3$ independent specimens). **l**, XRD patterns showing a shift of the primary collagen-related peak from $2\theta = 20.5°$ to 21.9° in CMpA, consistent with altered local packing or intermolecular environment. **m**, Fourier-transform infrared spectroscopy (FTIR) highlighting hydrogen-bonding reorganization and polysaccharide-environment reorganization in CMpA. **n**, Thermogravimetric analysis and derivative thermogravimetry curves showing enhanced thermal stability of CMpA relative to CM.

surface-level traits, such as zeta potential and rheology, with macroscopic wettability and tensile strength. Collectively, these measurements link interfacial and precursor-state changes with macroscopic mechanical response.

Interfacial reorganization was accompanied by coordinated changes in mesoscale physicochemical and mechanical behaviour[40]. Compared with CM, CMpA exhibited increased surface potential, rheological resistance and surface hydrophobicity, consistent with

https://doi.org/10.1038/s41893-026-01967-9

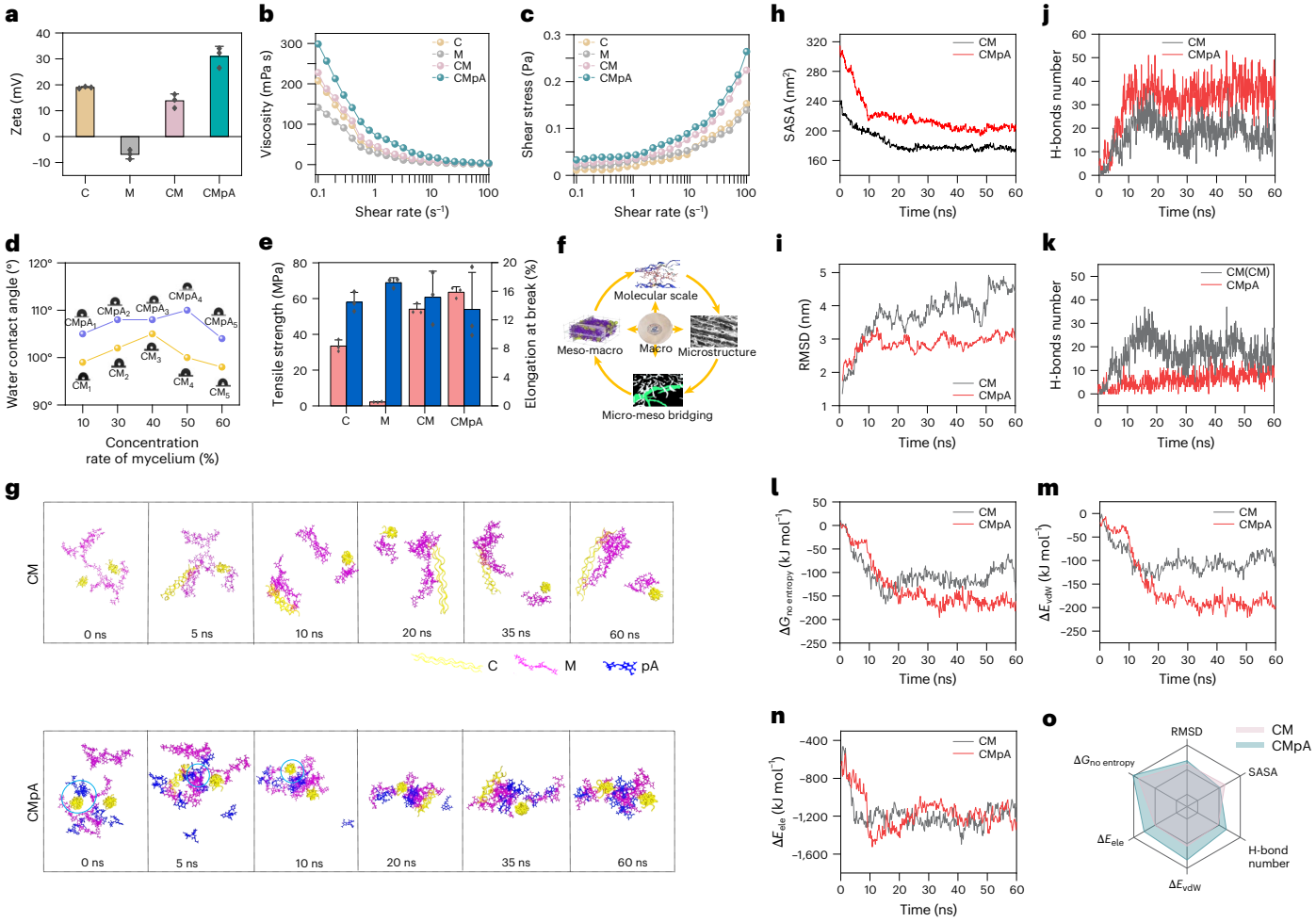


Fig. 3 | pA-mediated cross-scale mechanical reinforcement and local molecular interfacial association. a–**e**, Correlative characterization linking interfacial regulation to macroscopic mechanical response. **a**, Zeta potential, indicating pA-mediated modulation of interfacial charge state. **b**,**c**, Viscosity (**b**) and shear stress (**c**) as a function of shear rate, showing enhanced flow resistance in CMpA. **d**, Static water contact angles, reflecting increased surface hydrophobicity and interfacial uniformity after pA incorporation. **e**, Tensile strength and elongation at break of the different formulations. Tensile strength and elongation at break were analysed separately using one-way analysis of variance (ANOVA) followed by Tukey's honestly significant difference (HSD) multiple-comparisons test. Obvious overall differences were observed for tensile strength ($P < 0.001$) and elongation at break ($P = 0.013$). Data in **a** and **e** are presented as mean ± s.d. ($n = 3$ independent specimens). **f**–**o**, MD analysis of local C–M and C–M–pA interfacial association. **f**, Schematic linking molecular interfacial association, microstructural organization and mechanical behaviour. **g**, Representative MD snapshots, showing dynamic C–M clustering in CM and pA-associated interfacial contacts in CMpA. **h**,**i**, SASA and RMSD profiles, indicating structural relaxation and quasi-stationary simulation behaviour. **j**,**k**, Total and direct C–M hydrogen-bond numbers, showing that pA increases overall hydrogen bonding while redistributing direct C–M contacts into mediator-associated C–pA and M–pA interactions. **l**–**n**, MM/PBSA-derived entropy-uncorrected apparent interaction-energy decomposition, including total, van der Waals (vdW) and electrostatic contributions, supporting enhanced local interfacial stabilization in CMpA. **o**, Normalized radar plot integrating structural and energetic descriptors. **p**, Schematic summary of the proposed cross-scale mechanism, illustrating anthocyanin-rich pA as a non-covalent interfacial mediator that promotes C–pA and M–pA contacts, improves local interfacial continuity and translates into mesoscale network consolidation and macroscopic mechanical reinforcement.

interfacial stabilization extending beyond electrostatic interactions and formation of a more consolidated network (Supplementary Figs. 8 and 9 and Note 2.1)[33,40–42]. These changes culminated in enhanced tensile strength from 54.08 MPa in CM to 63.55 MPa in CMpA without a pronounced loss of extensibility (Fig. 3e and Supplementary Fig. 10)[43,44]. Together with ESEM, CLSM and SAXS evidence, these results support a cooperative reinforcement mechanism in which local interfacial mediation, pore-wall consolidation and mesoscale orientational coherence

facilitate stress transfer across the heterogeneous C–M network (Supplementary Note 2)[40,45].

Molecular dynamics (MD) simulations were used to examine the atomistic basis of pA-mediated local heterointerfacial association and energetic stabilization (Fig. 3f–o)[33]. To isolate the dominant interfacial chemistry, we constructed chemically representative local models comprising a collagen triple-helical segment, mycelium-derived chitin/β-glucan motifs and malvidin-3-O-glucoside identified by liquid chromatography–tandem mass spectrometry (LC–MS/MS; Supplementary Fig. 11, Table 3 and Note 2.2). Whereas the binary C–M model formed a fluctuating association state, pA promoted more persistent C–pA and M–pA contacts through multipoint hydrogen bonding, polar association and aromatic-associated dispersion interactions, providing a local non-covalent mediation pathway across the heterointerface. Consistent with this interaction pattern, CMpA showed a more stable root-mean-square deviation (RMSD) profile, reduced solvent-accessible surface area and greater structural compactness, together with increased overall hydrogen bonding despite fewer direct C–M hydrogen bonds, consistent with a redistribution of local intermolecular interactions (Fig. 3g–i, and Supplementary Figs. 12 and 13 and Note 2.2). Energy decomposition further showed that CMpA exhibited more favourable entropy-uncorrected apparent interaction energy than CM, arising mainly from enhanced van der Waals contributions rather than dominant electrostatic stabilization (Fig. 3j–p)[33,46].

Importantly, this molecular interpretation was consistently supported across three independent initial configurations and extended 500-ns trajectories, while interaction-entropy analysis provided complementary assessment of interaction energetics over the equilibrated trajectory segment (Supplementary Figs. 14–19, Tables 5–8 and Note 2.3). Within the scope of representative chemical-motif models rather than complete atomistic reconstruction of macroscopic assembly, these results support pA-mediated stabilization of local C–M heterointerfacial association. Integrated with SPR, XPS, FTIR/CD, microscopy and SAXS evidence, these simulations establish a model–experiment link from local non-covalent heterointerfacial mediation to pore-wall consolidation, mesoscale lamellar orientational coherence and mechanical reinforcement in CMpA[47].

Mechanical modelling of load transfer and damage

To connect pA-associated interfacial reorganization with macroscopic mechanical behaviour, a cross-scale mechanical framework was established on the basis of the experimentally resolved CMpA architecture. Molecular-scale analyses indicated that pA participates in non-covalent association and local chemical-environment reorganization at collagen–mycelium contact regions. These interfacial features were incorporated into a higher-scale mechanical representation by reconstructing a representative volume element (RVE) from the observed CMpA microstructure (Fig. 4a). The reconstructed RVE preserved the main architectural characteristics of the biocomposite, including fibre-rich pathways, collagen–mycelium contact regions and mesoscale orientational features.

A coupled solid-mechanics/phase-field fracture framework was then implemented in COMSOL 6.2 to analyse load transfer and damage evolution[48]. To balance statistical representativeness with computational efficiency, the 3D network was decomposed into three orthogonal cross-sections (RVE_{xy}, RVE_{xz} and RVE_{yz}; Fig. 4b), enabling plane-resolved quantification of anisotropy (Supplementary Note 3)[49]. Because the reconstructed architecture represents mesoscale network features rather than the full macroscopic specimen, the plane-wise approximation was used as a computationally tractable approach for evaluating structural anisotropy and damage localization[50,51]. The validity of this approximation was further examined using matched and random 3D cut models. This framework was used to assess how structural continuity and anisotropy influence stress transfer and damage-localization tendencies in the experimentally informed network.

Von Mises stress contours under uniaxial loading revealed orientation-dependent load-transfer pathways within the reorganized CMpA network (Fig. 4c and Supplementary Fig. 19). Stress preferentially concentrated along fibre-rich collagen domains and collagen–mycelium interfaces, consistent with continuous load-bearing pathways (Supplementary Note 3.1). Compared with binary CM, CMpA exhibited greater stress-pathway connectivity, consistent with pA-mediated interfacial reorganization enhancing interfacial continuity and stress redistribution across the C–M network. Mycelium-associated alignment further contributed to anisotropic stress transfer (Fig. 4d,e), while load partitioning revealed a mesoscale hierarchy in which fiber-rich domains carried tensile stress and matrix-rich regions accommodated deformation and damage (Supplementary Note 3.2). Orientation averaging of the three sectional responses using a Voigt–Reuss–Hill-type treatment yielded an effective 3D response in close agreement with the experiment ($R^2 = 0.975$; Fig. 4f and Supplementary Table 9)[50,52]. Consequently, these results support a network-level load-sharing mechanism in which improved interfacial continuity, connected fiber-rich pathways and anisotropic structural organization contribute to the high strength and retained structural integrity of CMpA.

Phase-field simulations further revealed anisotropic, phase-selective damage evolution in CMpA, with damage localized predominantly in matrix-rich regions at ~11% strain while reinforcing phases remained comparatively preserved before orientation-dependent crack propagation[14,52,53]. These results support a cooperative damage-tolerance mechanism in which pA-mediated heterointerfacial continuity, pore-wall consolidation and anisotropic network organization jointly redistribute stress, delay localized damage accumulation and guide crack propagation. Model robustness and transferability were further supported by complementary validation analyses (Fig. 4l, and Supplementary Figs. 20–25, Tables 10–12 and Notes 3.3–3.6).

Collectively, these simulations provided a cross-scale mechanical interpretation linking pA-associated interfacial stabilization with mesoscale load transfer and macroscopic reinforcement trends (Fig. 4m)[54], whereby pA promoted a more-cohesive local interfacial configuration, continuous load-bearing pathways, delayed damage initiation and guided crack propagation, providing a versatile design route for high-performance sustainable bio-based composites.

Multiscale functional integration in bio-based materials

Building on the mechanistic insights into pA-mediated heterointerfacial reorganization, we translated the reorganized network into functional material architectures. Through low-temperature mixing and spontaneous organization, the stable CMpA interpenetrating network was processed into dense flexible films or 3D aerogels (Fig. 5a, and Supplementary Figs. 26–28 and Notes 1.8 and 4.1). The persistence of the network across these processing routes indicated that the pA-mediated interfacial architecture was not restricted to a single material format but could be retained in both dense and porous structures. Collagen provided the structural scaffold, mycelium contributed hydrophobic and bioactive characteristics, and pA acted as a non-covalent interfacial mediator with stimuli-responsive functionality (Fig. 5b,c and Extended Data Table 1). CMpA exhibited increased surface hydrophobicity and a compact layered morphology, together with strong optical and mass-transport barrier performance, including 11% UV transmittance at 280–400 nm, while retaining 80% visible-light transmittance at 600 nm, as well as reduced water vapour permeability (WVP), oxygen transmission rate (OTR) and oxygen permeability (Fig. 5d–i). The physicochemical origins and formulation-level comparisons underlying these surface, optical and barrier properties are detailed in Supplementary Note 4.2 (refs. 55,56).

The same ternary integration also supported biofunctional performance. M, C and pA each exhibited intrinsic antioxidant activity, and CMpA achieved radical-scavenging efficiencies above 90%, with pA

https://doi.org/10.1038/s41893-026-01967-9

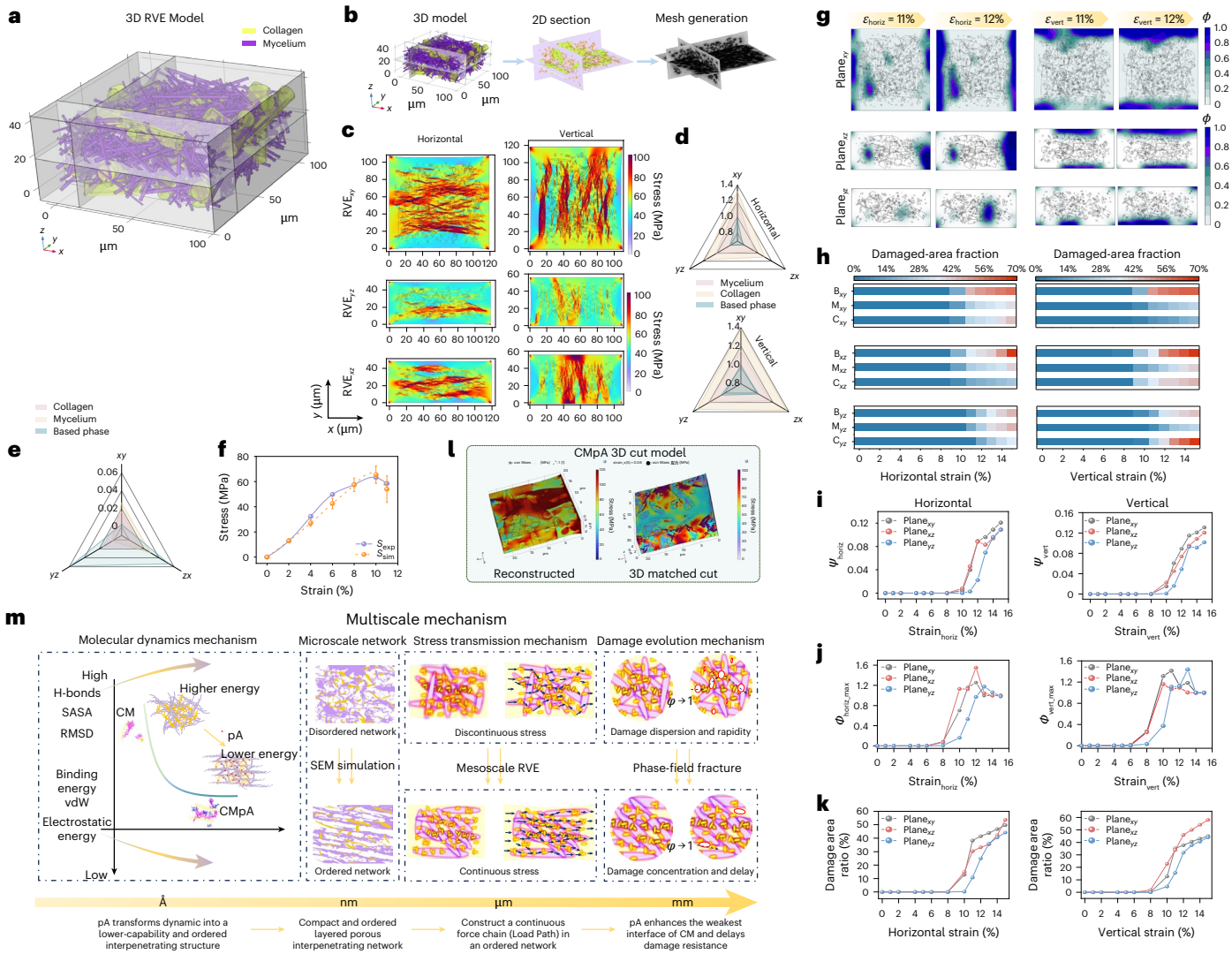


Fig. 4 | Mesoscale load transfer, anisotropic mechanics and damage evolution in the CMpA interpenetrating network. a,**b**, RVE construction. **a**, 3D RVE reconstructed from the experimentally resolved CMpA architecture. **b**, Orthogonal sections, RVE_{xy}, RVE_{xz} and RVE_{yz}, used for mesoscale mechanical and fracture analysis. **c**–**e**, Load-bearing hierarchy and anisotropy. **c**, Von Mises stress contours showing stress redistribution along collagen-rich fibres and collagen–mycelium interfacial regions. **d**, Standardized stress-bearing radar plots under horizontal and vertical stretching. **e**, Component load-bearing coefficients on the 3 principal planes. Matrix, mycelium and collagen fibres are shown in green, pink and yellow, respectively. **f**, Simulated and experimental stress–strain responses, showing good agreement of the RVE model with tensile behaviour ($R^2 = 0.975$). The experimental curve represents a single tensile measurement, whereas the simulated data are presented as mean ± s.d. from 3 simulated RVE sections. **g**,**h**, Phase-field damage analysis. **g**, Damage distribution at the critical strain. **h**, Damaged-area fraction across the *xy*, *xz* and *yz* planes, showing preferential matrix damage while collagen fibres and interfacial regions remain largely preserved. **i**–**k**, Damage-evolution analysis. The phase-field variable ϕ ranges from 0, undamaged, to 1, fully fractured. Crack-driving force and phase-field evolution reveal direction-dependent damage propagation and delayed crack percolation. **l**, CMpA 3D cut-model benchmark for evaluating the plane-wise RVE approximation. **m**, Multiscale mechanism linking pA-mediated interfacial reorganization to continuous load transfer, delayed damage localization and guided crack propagation.

and mycelium-derived components providing the major polyphenolic and bioactive contributions (Fig. 5j and Supplementary Fig. 33a)[55,57], whereas this level of enhancement was not observed in the binary MpA system (Supplementary Fig. 33b)[41]. This suggests that the ternary network helped retain, disperse and expose polyphenolic moieties more effectively within the composite. Similarly, CMpA achieved over 99% antibacterial efficiency against *Escherichia coli* and *Staphylococcus aureus*, whereas individual components showed only moderate inhibition (Fig. 5k,l and Supplementary Fig. 34a). ESEM imaging revealed collapsed bacterial cells and severely deformed envelopes after CMpA treatment, which is consistent with the antibacterial contribution of pA and mycelium-derived bioactive components (Fig. 5m and Supplementary Fig. 34b). The antibacterial response is primarily associated with the intrinsic bioactive chemistry of pA and mycelium-derived components, while the reorganized CMpA network may facilitate the spatial distribution and local presentation of antimicrobial moieties and provide an auxiliary barrier contribution through its more continuous pore-wall structure and restricted mass transport. These results indicate that the biofunctional performance of CMpA arises from the coupling of component-intrinsic bioactive chemistry with architecture-assisted functional expression, rather than from an ordering-only mechanism[41].

To assess packaging relevance, we benchmarked CMpA against representative food-packaging films using an Ashby-style plot (Fig. 5n, and Supplementary Table 13 and Note 4.3). Relative to conventional mycelium-, protein- and PVA-based films, CMpA occupied the

https://doi.org/10.1038/s41893-026-01967-9

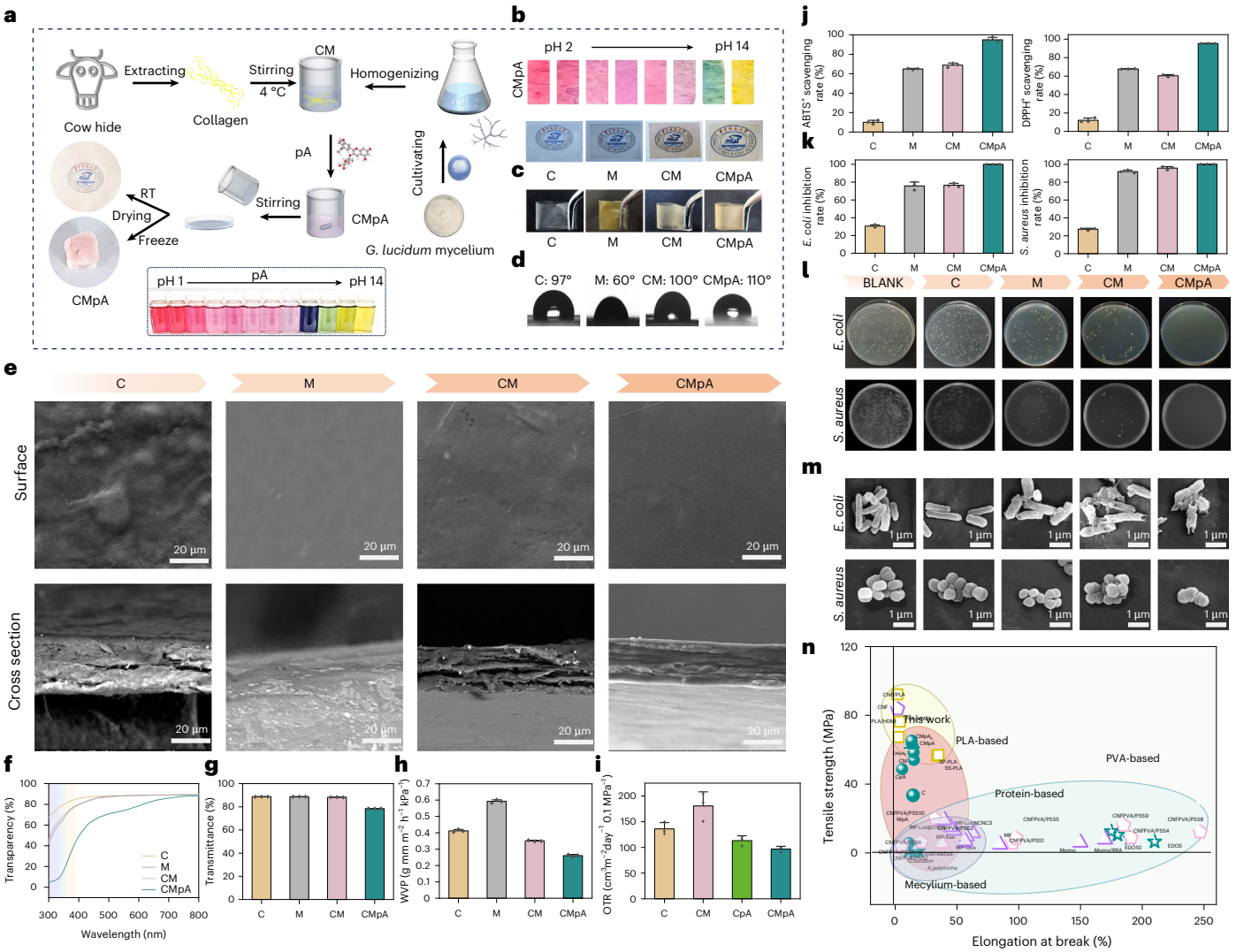


Fig. 5 | Fabrication and multifunctional performance of pA-mediated ternary biocomposite films. a, Schematic illustration of the fabrication strategy for the ternary composite CMpA, showing pA-mediated interfacial association within the CM matrix and its processability into films or aerogels. **b**, Photographs of CMpA films under different pH conditions, demonstrating uniform and reversible colourimetric response. **c**, Digital images showing flexibility and mechanical integrity of CMpA films under bending. **d**, Static water contact angles, indicating enhanced surface hydrophobicity associated with pA-mediated ternary interfacial reorganization and surface/network consolidation. **e**, ESEM images of surfaces and cross-sections of C, M, CM and CMpA films, highlighting the densely aligned architecture in CMpA. **f**,**g**, UV–Vis spectra (**f**) and visible-light transmittance (**g**), showing strong UV shielding with maintained optical transparency in CMpA. **h**, Water vapour permeability (WVP), demonstrating reduced permeability in the ternary network. **i**, Oxygen transmission rate (OTR) of different films. The reduced OTR of CMpA indicates improved oxygen-barrier performance, consistent with the formation of a denser and more tortuous ternary network. **j**, Antioxidant activity assessed by 2,2′-azino-bis(3-ethylbenzothiazoline-6-sulfonic acid) (ABTS) and 2,2-diphenyl-1-picrylhydrazyl (DPPH) assays, showing high radical-scavenging efficiency in CMpA. **k**, Antibacterial performance against *E. coli* (left) and *S. aureus* (right), quantified by inhibition efficiency and colony-counting images, respectively. **l**,**m**, Colony plate diagram (**l**) and ESEM images (**m**) of bacteria after treatment, revealing severe membrane disruption in the CMpA group. **n**, Ashby plot comparing tensile strength and elongation at break of CMpA with representative packaging films from the literature, illustrating high tensile strength with retained moderate deformability enabled by pA-mediated heterointerfacial reorganization. Data in **g**–**k** are presented as mean ± s.d. ($n = 3$ independent specimens). Scale bars, 20 μm (**e**) and 1 μm (**m**).

high-strength/high-ductility regime. Compared with CM, it achieved a tensile strength of 63.55 MPa while retaining 12% elongation[41]. Combined with intrinsic bioactivity, UV shielding, low water vapour permeability, antioxidant activity and broad-spectrum antibacterial performance, CMpA emerged as a promising sustainable multifunctional active-packaging material[58].

Active preservation and freshness indication

To evaluate the multifunctional feasibility of pA-mediated CMpA films, we assessed the active protection and intelligent freshness indication performance of ternary CMpA film in food preservation[59,60]. Strawberries and fish fillets are particularly vulnerable to microbial spoilage and the accumulation of total volatile nitrogen compounds during storage[59]. The CMpA film integrated barrier protection, intrinsic antibacterial activity and pH-responsive visual signalling within a single material platform, making it suitable for evaluating simultaneous preservation and freshness indication in strawberry and fish models.

The pH responsiveness of the CMpA film was analysed by colourimetric analysis. The colour parameters revealed clear differences among film types (Extended Data Table 1 and Supplementary Table 14). C and M films remained chromatically stable, while the disordered CM film showed irregular and poorly reproducible shifts in b^* (yellow–blue colour coordinate) and ΔE (total colour difference) values. CMpA films exhibited strong, reversible and reproducible colour transitions upon

pH variation, indicating that pA-mediated ternary network organization helped retain robust pH responsiveness[14]. By contrast, the MpA film showed only minimal colour change, suggesting that unregulated association in the absence of the collagen-guided ternary interface limited the pH-responsive transformation of pA (Supplementary Table 14). Thus, the reorganized ternary network in CMpA helped retain the sensing activity of pA while embedding it within a mechanically robust composite framework.

We then evaluated preservation performance under realistic conditions. CMpA-wrapped strawberries best maintained their appearance after 13 days compared with the other groups, exhibiting minimal dehydration and no obvious visible microbial spoilage (Fig. 6a). Other ternary formulations also showed preservation effects during 13-day storage, although CMpA showed the most favourable overall performance (Supplementary Fig. 35a). Comparing the loss in weight of these samples, the strawberries wrapped with CMpA showed the lowest moisture loss (Fig. 6d). Crucially, this preservation effect indicated that the consolidated CMpA network helped maintain the local storage microenvironment, while its pH-responsive colourimetric behaviour enabled simultaneous food protection and freshness indication.

Subsequently, we evaluated the freshness preservation of fish fillets, as a more demanding spoilage model characterized by rapid microbial growth and nitrogen release[61]. After 5 days, CMpA-wrapped samples maintained superior colour and tissue integrity compared to controls (Fig. 6b and Supplementary Fig. 35b), and showed the lowest mass loss similar to the strawberry preservation test (Fig. 6e). In the real-time visual freshness-monitoring test, the CMpA film displayed a distinct colour shift from pink to bluish-purple in response to spoilage-induced pH elevation (Fig. 6c), as further supported by ΔE analysis (Supplementary Table 15, and Fig. 6e). Compared to the control tests, this responsiveness was well-preserved in the CMpA and CpA films but was markedly absent in the MpA system (Supplementary Fig. 36). The limited response of MpA suggests that, without collagen-associated structural regulation, pA tends to undergo less controlled aggregation or shielding of responsive sites, thereby reducing pH-induced chromatic transformation.

Quantitative freshness indices further confirmed the preservation efficacy of CMpA. During strawberry storage, the blank group showed a rapid pH increase and pronounced total soluble solids (TSS) fluctuation, indicating accelerated organic acid consumption, ripening and sugar metabolism. In contrast, CMpA-wrapped strawberries showed the slowest pH increase and a more stable TSS profile over 13 days, consistent with reduced weight loss and delayed visible spoilage (Fig. 6f and Supplementary Fig. 37a,b). For fish fillets, the blank and binary-film groups displayed marked pH elevation and rapid total volatile basic nitrogen (TVB-N) accumulation, reflecting protein degradation and formation of ammonia and volatile amines. CMpA substantially suppressed both pH increase and TVB-N formation, maintaining the lowest spoilage indices among all groups (Fig. 6g and Supplementary Fig. 37c,d). These results show that the CMpA network integrates barrier protection, delays metabolic and microbial deterioration, and provides real-time freshness monitoring (Fig. 6h and Supplementary Note 4.4).

The pA-mediated interfacial strategy was further translated from films to oriented porous aerogels, enabling fluid management and rapid haemostasis within 30 s while maintaining blood compatibility (Extended Data Fig. 1, and Supplementary Note 5 and Figs. 38 and 39)[62–64]. More broadly, the CMpA system provides a mechanism-guided platform that links molecular/interfacial regulation with macroscale utility. Its functional translation was demonstrated in active-packaging films and haemostasis-related porous aerogels, while the same structural principle may provide a basis for future exploration of adsorption- or remediation-related applications.

Discussion

This study addresses interfacial decoupling and stochastic entanglement as key barriers to structural cohesion in heterogeneous biopolymer networks. Using the collagen–mycelium–anthocyanin system as a representative model, we showed that plant-derived anthocyanins (pA) act as multivalent non-covalent mediators to reorganize collagen–mycelium (C–M) heterointerfaces. Multiscale experiments, simulations and mechanical modelling linked this local regulation to improved interfacial continuity and lamellar organization, establishing a cross-scale pathway from small-molecule-mediated heterointerfacial reorganization to mesoscale architectural continuity, mechanical robustness and functional integration in CMpA.

At the molecular and interfacial levels, convergent simulation, spectroscopic and interfacial evidence suggest that pA redistributes multivalent non-covalent interactions across C–M heterointerfaces rather than inducing new covalent structures or de novo collagen fibrillogenesis. At the mesoscale, this regulation is associated with increased interfacial continuity, anisotropy and lamellar coherence without molecular-scale periodic ordering. Together, these findings identify chemically selective interfacial compatibility, rather than bulk compositional modification or long-range molecular order, as a key determinant of structural coherence in heterogeneous biopolymer networks.

The mechanical enhancement of CMpA is closely associated with this reorganized architecture. CMpA reached a tensile strength of 63.55 MPa, while finite-element and phase-field simulations linked the continuous lamellar pore-wall network to more connected load-transfer pathways, reduced local stress concentration and delayed damage localization. These results identify interfacial continuity and mesoscale organization, rather than composition alone, as key determinants of mechanical reliability.

This interfacial reorganization strategy further enables multifunctional integration across material formats. CMpA films provided a sustainable, active and intelligent packaging prototype based on mild aqueous processing without covalent crosslinkers or harsh chemical treatments and on naturally derived components, including collagen-rich by-products, cultivable fungal mycelium and plant-derived anthocyanins. The same C–M–pA chemistry was translated into porous aerogels supporting high liquid uptake, blood confinement and rapid haemostasis with low haemolysis. Unlike lamellar materials generated by freeze-induced lamellation, nanofibril alignment, external-field orientation or multilayer assembly, CMpA developed mesoscale lamellar coherence through pA-mediated non-covalent reorganization of pre-formed C–M heterointerfaces under mild processing conditions (Supplementary Table 16 and Note 5.3). This mechanism-guided strategy therefore provides a design route for selected heterogeneous biopolymer interfaces in which multivalent hydrogen bonding, aromatic interactions and interfacial compatibility can be coordinated.

More broadly, small-molecule-mediated heterointerfacial regulation offers a route to reconcile chemical heterogeneity with structural integration in bio-based composites. The CMpA framework further distinguished architecture-dependent mechanical and transport properties from component-intrinsic bioactivity, enabling multifunctional integration without attributing antioxidant, antibacterial, UV-shielding or pH-responsive behaviour directly to structural reorganization. Its translation from dense films to porous, blood-compatible aerogels further supports the applicability of this interface-mediated design principle across distinct material formats.

Future work should advance this proof-of-concept framework towards spatially resolved, wet-state and application-specific understanding of the interfacial mechanism. Interface-sensitive mapping under hydrated and deformed conditions could clarify the distribution, retention and dynamic association of pA within buried C–M interfaces. Packaging translation requires systematic

https://doi.org/10.1038/s41893-026-01967-9

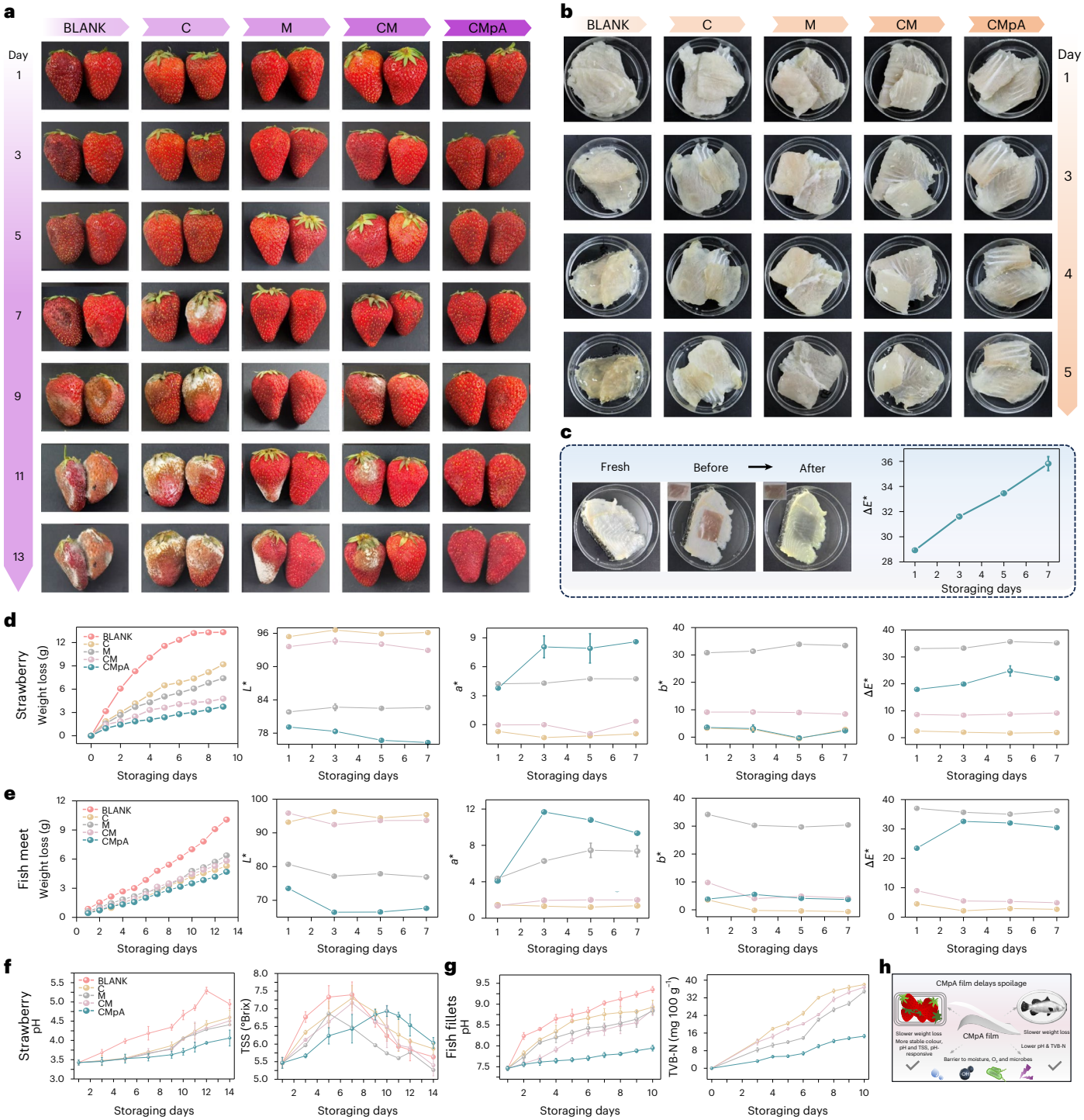


Fig. 6 | Fresh-food preservation and freshness indication enabled by CMpA biocomposite films. a, Photographs of strawberries stored for 1–13 days in different films, showing delayed dehydration and visible spoilage in the CMpA group. **b**, Appearance of fish fillets during 1–5 days of storage, showing improved colour and texture retention with CMpA packaging. **c**, Time-dependent pH-triggered colourimetric response of CMpA films during fish storage, arising from spoilage-induced pH elevation associated with volatile nitrogen compounds. **d**, Mass loss and colourimetric parameters (L^*, lightness; a^*, red–green colour coordinate; b^* and ΔE) of strawberries, indicating reduced moisture loss and slower chromatic deterioration with CMpA. **e**, Mass loss and colourimetric parameters of fish fillets, showing enhanced mass retention and pronounced ΔE evolution in response to spoilage-related chemical changes. **f**, Changes in pH and total soluble solids (TSS) of strawberries during storage, showing that CMpA slowed physicochemical deterioration. **g**, Changes in pH and total volatile basic nitrogen (TVB-N) of fish fillets, showing that CMpA suppressed pH elevation and TVB-N accumulation, consistent with delayed protein degradation and spoilage. **h**, Schematic illustration of the preservation mechanism, in which the consolidated CMpA ternary network integrates UV shielding, oxygen and moisture barrier properties, antioxidant activity and antibacterial effects to delay microbial growth, oxidative deterioration and quality loss while enabling real-time freshness indication. Data in **c**–**e** are presented as mean ± s.d. ($n = 3$ spatial measurements at different positions on the same specimen); data in **f**, **g** are presented as mean ± s.d. ($n = 3$ independent specimens).

evaluation of moisture durability, humidity-dependent barrier performance, migration, food-contact safety, cost performance and scalable processing, whereas biomedical extension requires in vivo wound-closure, histological and inflammatory-response studies. Building on the mediator-screening and extension-system experiments performed here, systematic structure–function mapping should encompass defined anthocyanins, related polyphenols, other interaction-site-bearing small molecules and additional mismatched biopolymer pairs. Chemically matching hydrogen-bonding, aromatic, ionic, coordination or redox-active motifs may further extend this selective strategy beyond food preservation and haemostasis to environmental remediation, sustainable agriculture, green construction and biodegradable filtration/separation.

Methods

Fabrication of CMpA ternary composite films

Experimental materials, including *G. lucidum* mycelium (M), collagen (C) and plant-derived anthocyanins (pA), were sourced and prepared as described in the Supplementary Methods. CMpA ternary composite films were fabricated through a pA-mediated non-covalent interfacial assembly strategy. Briefly, mycelium and collagen were dispersed in water according to the designed formulation, followed by the introduction of pA as a multivalent interfacial mediator. Binary CM and ternary CMpA films were obtained by aqueous dispersion casting and controlled drying. The detailed formulations, component ratios, preparation sequences and macroscopic appearances of the binary CM and ternary CMpA films are provided in Supplementary Table 1 and Supplementary Fig. 1.

Microstructural and orientation characterization

The multiscale architecture of the composite films was characterized using optical microscopy, ESEM (JEOL JSM-IT510) and CLSM. To quantify interfacial coupling and structural ordering, orientational metrics were derived from the ESEM micrographs using customized image-analysis scripts. Herman's orientation factors (S) were calculated to quantify the degree of preferential orientation of fibrillar motifs, as detailed in the Supplementary Information. Crystallographic features were analysed via X-ray diffraction (XRD; Rigaku Ultima IV), and the chemical interactions were elucidated through FTIR and UV–Vis spectroscopy (SolidSpec-3700, Shimadzu).

MD simulations

All-atom MD simulations were performed using GROMACS 2018.8 to examine local non-covalent interactions at the C–M heterointerface in CMpA. Reduced representative interfacial models were constructed using a collagen segment (PDB ID 7CWK), chitin/β-1,3-glucan oligomers to represent mycelium-side motifs, and malvidin-3-O-glucoside as the representative pA molecule identified by LC–MS/MS. The collagen segment was described with AMBER14SB protein force field, whereas pA and non-protein oligomers were parameterized using General AMBER Force Field (GAFF) with restrained electrostatic potential (RESP)-derived charges. Systems were solvated with TIP3P water, neutralized with Na^+, energy minimized and equilibrated under NVT/NPT ensembles. Primary 10-mer models were simulated for 500 ns, with additional reduced 4-mer replicate models used to assess robustness. The RMSD, solvent-accessible surface area (SASA), hydrogen bonds, contacts and molecular mechanics/Poisson–Boltzmann surface area (MM/PBSA)-derived entropy-uncorrected apparent interaction energies of all trajectories were analysed. Detailed protocols are provided in the Supplementary Methods.

RVE construction and finite-element analysis

To bridge the microscopic topology with macroscopic mechanical performance, a high-fidelity 3D representative volume element (RVE) was developed. Adhering to the Hill–Mandel macro-homogeneity condition, RVE dimensions (110 μm × 110 μm × 50 μm) were calibrated on the basis of quantitative ESEM analysis to ensure statistical representativeness. A customized stochastic sequential expansion algorithm was employed to reconstruct the interpenetrating networks. Mechanical responses and damage evolution were simulated using a phase-field fracture formulation in COMSOL Multiphysics 6.2. Detailed protocols are provided in the Supplementary Methods.

Reporting summary

Further information on research design is available in the Nature Portfolio Reporting Summary linked to this article.

Data availability

All data supporting the findings of this study are available within the Article and its Supplementary Information. Source data are provided with this paper.

Code availability

The code used for this study is available on Zenodo at https://doi.org/10.5281/zenodo.22152550 (ref. 65).

References

1. Munch, E. et al. Tough, bio-inspired hybrid materials. *Science* **322**, 1516–1520 (2008).
2. Huang, W. et al. Multiscale toughening mechanisms in biological materials and bioinspired designs. *Adv. Mater.* **31**, 1901561 (2019).
3. Liu, Z., Zhang, Z. & Ritchie, R. O. Structural orientation and anisotropy in biological materials: functional designs and mechanics. *Adv. Funct. Mater.* **30**, 1908121 (2020).
4. Zhang, M. et al. On the damage tolerance of 3-D printed Mg-Ti interpenetrating-phase composites with bioinspired architectures. *Nat. Commun.* **13**, 3247 (2022).
5. Liu, W. C., Chou, V. H. Y., Behera, R. P. & Le Ferrand, H. Magnetically assisted drop-on-demand 3D printing of microstructured multimaterial composites. *Nat. Commun.* **13**, 5015 (2022).
6. Li, T. et al. Anisotropic, lightweight, strong, and super thermally insulating nanowood with naturally aligned nanocellulose. *Sci. Adv.* **4**, eaar3724 (2018).
7. Dong, X. et al. Low-value wood for sustainable high-performance structural materials. *Nat. Sustain.* **5**, 628–635 (2022).
8. Tardy, B. L. et al. Advancing bio-based materials for sustainable solutions to food packaging. *Nat. Sustain.* **6**, 360–367 (2023).
9. Yu, L. et al. Molecular self-assembly strategy tuning a dry crosslinking protein patch for biocompatible and biodegradable haemostatic sealing. *Nat. Commun.* **16**, 1437 (2025).
10. Wu, Y. et al. Revivable self-assembled supramolecular biomass fibrous framework for efficient microplastic removal. *Sci. Adv.* **10**, eadn8662 (2024).
11. Kamada, A. et al. Controlled self-assembly of plant proteins into high-performance multifunctional nanostructured films. *Nat. Commun.* **12**, 3529 (2021).
12. Shin, Y. & Brangwynne, C. P. Liquid phase condensation in cell physiology and disease. *Science* **357**, eaaf4382 (2017).
13. Liu, J. X. et al. Liquid–liquid phase separation within fibrillar networks. *Nat. Commun.* **14**, 6085 (2023).
14. Shen, Z. H. et al. Phase-field modeling and machine learning of electric–thermal–mechanical breakdown of polymer-based dielectrics. *Nat. Commun.* **10**, 1843 (2019).
15. He, G., Dahl, T., Veis, A. & George, A. Nucleation of apatite crystals in vitro by self-assembled dentin matrix protein 1. *Nat. Mater.* **2**, 552–558 (2003).
16. Liu, Y. et al. Intrafibrillar collagen mineralization produced by biomimetic hierarchical nanoapatite assembly. *Adv. Mater.* **23**, 975–980 (2011).

17. Kang, X. et al. Lignin–polysaccharide interactions in plant secondary cell walls revealed by solid-state NMR. *Nat. Commun.* **10**, 347 (2019).
18. Yang, G., Gong, Z., Luo, X., Chen, L. & Shuai, L. Bonding wood with uncondensed lignins as adhesives. *Nature* **621**, 511–515 (2023).
19. Vanholme, R., Demedts, B., Morreel, K., Ralph, J. & Boerjan, W. Lignin biosynthesis and structure. *Plant Physiol.* **153**, 895–905 (2010).
20. Häkkinen, L. et al. A role for decorin in the structural organization of periodontal ligament. *Lab. Invest.* **80**, 1869–1880 (2000).
21. Fang, J. et al. Decoding the mechanical characteristics of the human anterior cruciate ligament entheses through graduated mineralization interfaces. *Nat. Commun.* **15**, 9253 (2024).
22. Eder, M., Amini, S. & Fratzl, P. Biological composites—complex structures for functional diversity. *Science* **362**, 543–547 (2018).
23. Hughes, M. P. et al. Atomic structures of low-complexity protein segments reveal kinked β sheets that assemble networks. *Science* **359**, 698–701 (2018).
24. Sinha, A. et al. Living fiber dispersions from mycelium as a new sustainable platform for advanced materials. *Adv. Mater.* **37**, 2418464 (2025).
25. Noji, M., Sugita, Y., Yamazaki, Y., Miyazaki, M. & Suzuki, Y. Protein design of two-component tubular assemblies similar to cytoskeletons. *Nat. Commun.* **16**, 6738 (2025).
26. Cheng, Q. et al. Molecular architecture of chitin and chitosan-dominated cell walls in zygomycetous fungal pathogens by solid-state NMR. *Nat. Commun.* **15**, 8295 (2024).
27. Fernando, L. D. et al. Structural adaptation of fungal cell wall in hypersaline environment. *Nat. Commun.* **14**, 7082 (2023).
28. Mohammadi, P. et al. Biomimetic composites with enhanced toughening using silk-inspired triblock proteins and aligned nanocellulose reinforcements. *Sci. Adv.* **5**, eaaw2541 (2019).
29. Yang, D. et al. Immunomodulatory multifunctional janus collagen-based membrane for advanced bone regeneration. *Nat. Commun.* **16**, 4264 (2025).
30. Trouillas, P. et al. Stabilizing and modulating color by copigmentation: insights from theory and experiment. *Chem. Rev.* **116**, 4937–4982 (2016).
31. Yang, R. et al. Non-covalent binding of cyanidin-3-*O*-glucoside onto peanut oil body for improved stability: molecular interactions and properties. *Food Chem.* **484**, 144384 (2025).
32. Zhu, B. et al. Boosting membrane carbon capture via multifaceted polyphenol-mediated soldering. *Nat. Commun.* **14**, 1697 (2023).
33. Han, Y. et al. Polyphenol-mediated assembly of proteins for engineering functional materials. *Angew. Chem. Int. Ed.* **59**, 15618–15625 (2020).
34. Sorushanova, A. et al. The collagen suprafamily: from biosynthesis to advanced biomaterial development. *Adv. Mater.* **31**, 1801651 (2019).
35. Shannon, C. E. A mathematical theory of communication. *Bell Syst. Tech. J.* **27**, 379–423 (1948).
36. Zhang, J., Zhang, M., Wan, H., Zhou, J. & Lu, A. Coordinatively stiffen and toughen polymeric gels via the synergy of crystal-domain cross-linking and chelation cross-linking. *Nat. Commun.* **16**, 320 (2025).
37. Wang, H. et al. Fabrication of living entangled network composites enabled by mycelium. *Adv. Sci.* **11**, e2309370 (2024).
38. Li, X., Yang, J., Khan, M. R., Ahmad, N. & Zhang, W. Dopamine-polyphenol self-assembled nanoparticle functionalized soy protein isolate films. *Chem. Eng. J.* **524**, 169424 (2025).
39. Liu, W. et al. Hydrogen-bonding enhanced anion exchange membrane for high performance alkaline water electrolysis. *Adv. Energy Mater.* **15**, e03110 (2025).
40. Bian, T. et al. Electrostatic co-assembly of nanoparticles with oppositely charged small molecules into static and dynamic superstructures. *Nat. Chem.* **13**, 940–949 (2021).
41. Xue, S. et al. Polyphenol-based functional materials: structural insights, composite strategies, and biomedical applications. *Adv. Sci.* **12**, e08924 (2025).
42. Alshareedah, I., Moosa, M. M., Pham, M., Potoyan, D. A. & Banerjee, P. R. Programmable viscoelasticity in protein–RNA condensates with disordered sticker-spacer polypeptides. *Nat. Commun.* **12**, 6620 (2021).
43. Zhu, S. et al. Bioinspired structural hydrogels with highly ordered hierarchical orientations by flow-induced alignment of nanofibrils. *Nat. Commun.* **15**, 118 (2024).
44. Li, H. et al. Hierarchical crack-resistant, tissue-mimetic hydrogels enabled by progressive nanocrystallization of anisotropic polymer networks. *Nat. Commun.* **16**, 10890 (2025).
45. Tang, H. et al. High-strength, multi-mode processable bamboo molecular bioplastic enabled by solvent-shaping regulation. *Nat. Commun.* **16**, 8729 (2025).
46. Zhang, Z. et al. In-situ localised alignment assisted salting-out enhanced ionogels with high strength, toughness and impact resistance. *Nat. Commun.* **16**, 7683 (2025).
47. Wang, H., Wu, Z., Tao, J., Wang, B. & He, C. Bamboo-inspired crack-face bridging fiber reinforced composites simultaneously attain high strength and toughness. *Adv. Sci.* **11**, 2308070 (2024).
48. Li, H. et al. Van-der-Waals-forces-modulated graphene-*P*-phenyl-graphene carbon allotropes. *Nat. Commun.* **16**, 10011 (2025).
49. Murgas, B., Stickel, J., Brewer, L. & Ghosh, S. Modeling complex polycrystalline alloys using a Generative Adversarial Network enabled computational platform. *Nat. Commun.* **15**, 9441 (2024).
50. Hill, R. Elastic properties of reinforced solids: some theoretical principles. *Mech. Phys. Solids* **11**, 357–372 (1963).
51. Zhang, M. et al. Spontaneous alignment of graphene oxide in hydrogel during 3D printing for multistimuli-responsive actuation. *Adv. Sci.* **7**, 1903048 (2020).
52. Guo, X., Dong, X., Zou, G., Gao, H. & Zhai, W. Strong and tough fibrous hydrogels reinforced by multiscale hierarchical structures with multimechanisms. *Sci. Adv.* **9**, eadf7075 (2023).
53. Yu, S. et al. On the crack resistance and damage tolerance of 3D-printed nature-inspired hierarchical composite architecture. *Nat. Commun.* **15**, 9532 (2024).
54. Wang, X. Q., Jin, Z., Ravichandran, D. & Gu, G. X. Artificial intelligence and multiscale modeling for sustainable biopolymers and bioinspired materials. *Adv. Mater.* **37**, 2416901 (2025).
55. Yu, K., Dixon, R. A. & Duan, C. A role for ascorbate conjugates of (+)-catechin in proanthocyanidin polymerization. *Nat. Commun.* **13**, 3425 (2022).
56. Wu, X. et al. Heteroaromatic π-stacking engineered near-infrared absorption for highly stable near-zero transmittance electrochromic window. *Nat. Commun.* **16**, 9964 (2025).
57. Ma, Y., Morozova, S. M. & Kumacheva, E. From nature-sourced polysaccharide particles to advanced functional materials. *Adv. Funct. Mater.* **36**, 2312707 (2024).
58. Lundberg, D. J. et al. Nested non-covalent interactions expand the functions of supramolecular polymer networks. *Nat. Commun.* **15**, 3951 (2024).
59. Gantenbein, S. et al. Three-dimensional printing of mycelium hydrogels into living complex materials. *Nat. Mater.* **22**, 128–134 (2023).
60. Zhang, Z., Liang, L., Feng, J., Hou, G. & Ren, W. Significant enhancement of proton conductivity in solid acid at the monolayer limit. *Nat. Commun.* **15**, 2706 (2024).
61. Bhargava, N., Sharanagat, V. S., Mor, R. S. & Kumar, K. Active and intelligent biodegradable packaging films using food and food waste-derived bioactive compounds: a review. *Trends Food Sci. Tech.* **105**, 385–401 (2020).

62. Wang, Y. et al. A shape-recovery polycationic fibroin for hemostasis-regeneration transition by recapitulating natural coagulation networks. *Adv. Mater.* **37**, e12265 (2025).
63. Fang, Y. et al. Blood-triggered self-sealing and tissue adhesive hemostatic nanofabric. *Nat. Commun.* **16**, 4910 (2025).
64. Shahriar, S. M. S. et al. Bicomponent nano- and microfiber aerogels for effective management of junctional hemorrhage. *Nat. Commun.* **16**, 2403 (2025).
65. Xie, S. & Tunuhe, A. CMpA RVE generation code (version 1.0.0) [Computer software]. *Zenodo* https://doi.org/10.5281/zenodo.22152550 (2026).

Acknowledgements

We thank the HUST–Shenguan Joint Research Center of Synthetic Biology for its institutional support of this work.

Author contributions

S.X., Y. Zhou and H.Y. conceived and supervised this work. S.X. and A.T. designed the experiments. A.T. performed the major experiments and data analyses. Z.Z. conducted antibacterial tests and produced schematic diagrams. K.Z. carried out the MD calculations. A.T. drafted the manuscript. S.X., H.Y., F.M., Y. Zhao, J.S. and Y.G. reviewed the manuscript. S.X. revised the manuscript. All authors were actively involved in discussion, analysis and revision.

Funding

The authors declare no relevant funding.

Competing interests

The authors declare no competing interests.

Additional information

Extended data is available for this paper at https://doi.org/10.1038/s41893-026-01967-9.

Supplementary information The online version contains supplementary material available at https://doi.org/10.1038/s41893-026-01967-9.

Correspondence and requests for materials should be addressed to Hongbo Yu, Yaxian Zhou or Shangxian Xie.

Peer review information *Nature Sustainability* thanks Wei Lin and the other, anonymous, reviewers for their contribution to the peer review of this work.

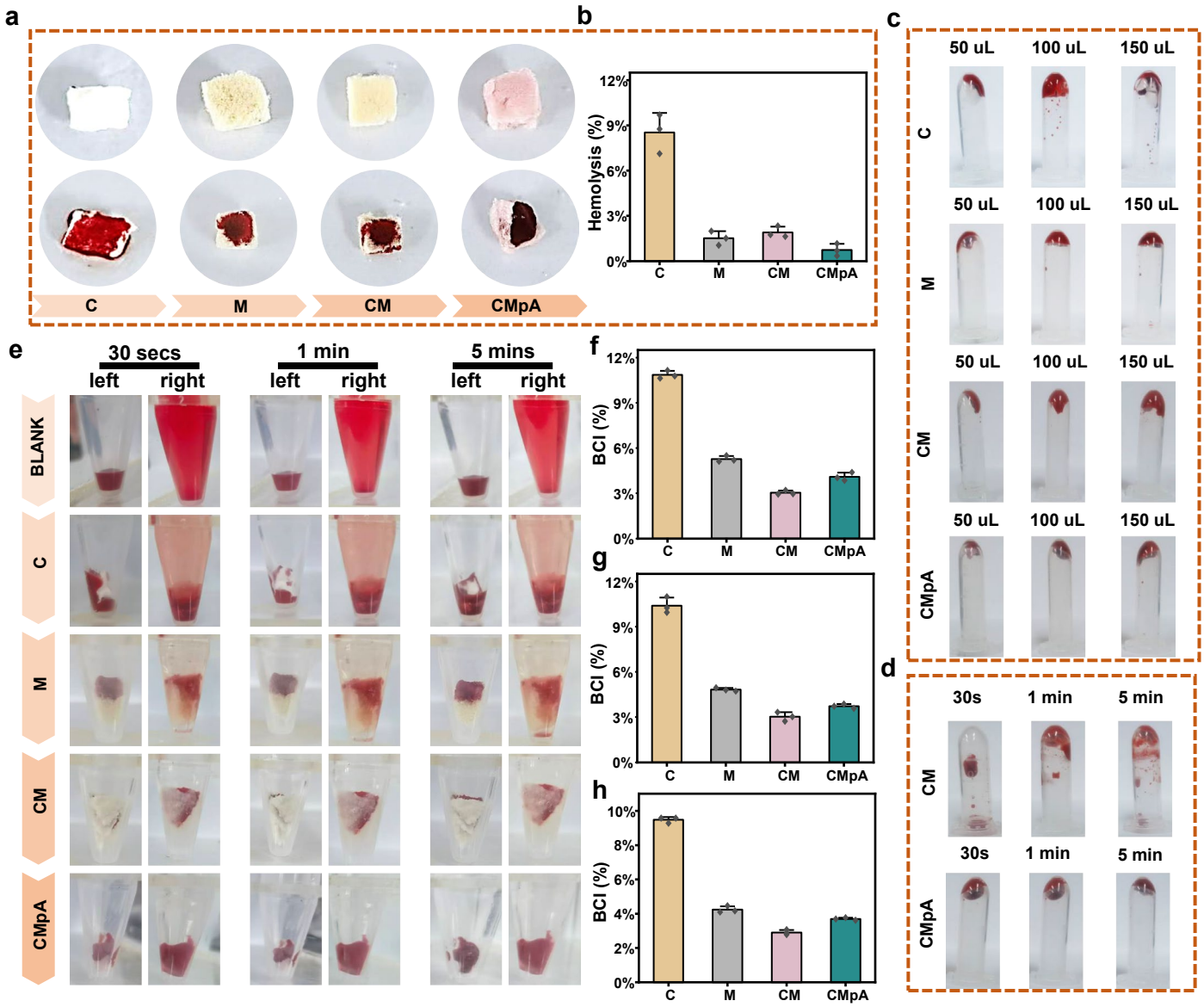
Reprints and permissions information is available at www.nature.com/reprints.

Publisher's note Springer Nature remains neutral with regard to jurisdictional claims in published maps and institutional affiliations.

Springer Nature or its licensor (e.g. a society or other partner) holds exclusive rights to this article under a publishing agreement with the author(s) or other rightsholder(s); author self-archiving of the accepted manuscript version of this article is solely governed by the terms of such publishing agreement and applicable law.

© The Author(s), under exclusive licence to Springer Nature Limited 2026

https://doi.org/10.1038/s41893-026-01967-9



Extended Data Fig. 1 | Hemocompatibility and rapid hemostatic performance of the CMpA aerogel. a, Representative images of whole-blood absorption upon contact with C, M, CM, and CMpA aerogels, showing rapid and complete uptake by CMpA. **b**, In vitro hemolysis ratios of different materials, with M, CM and CMpA remaining below the 5% safety threshold and CMpA exhibiting minimal hemolysis. **c**, Maximum blood absorption capacity evaluated using increasing blood volumes within 2 min, highlighting the superior uptake ability of CMpA. **d**, Time required for CM and CMpA to completely absorb a fixed blood volume, demonstrating the accelerated kinetics of CMpA. **e**, Clot stability assessment after incubation with heparinized whole blood for 30 s, 1 min, and 5 min (left, before washing; right, after rinsing). **f**-**h**, Quantitative blood-clotting index (BCI) measured at 30 s (**f**), 1 min (**g**), and 5 min (**h**), where lower values indicated faster and more stable clot formation; CMpA consistently showed the lowest BCI. Overall, the CMpA aerogel integrated rapid capillary-driven blood uptake with stable biointerfaces, enabling synergistic physical sequestration and accelerated coagulation for fast and hemocompatible hemostasis. Data in **b** and **f**–**h** are presented as mean ± s.d. (n = 3 independent specimens).

https://doi.org/10.1038/s41893-026-01967-9

Extended Data Table 1 | Color parameters of CMpA films in pH solutions

pH[a]	L^*[b]	a^*[c]	b^*[d]	ΔE[e]	film[f]
1	60.72±0.08[h]	48.48±0.21[a]	-4.57±0.01[f]	60.77±0.17[a]	
2	74.62±0.18[d]	9.93±0.01[b]	6.78±0.02[d]	24.76±0.17[d]	
4	72.07±0.26[f]	9.54±0.01[c]	7.37±0.06[c]	27.01±0.25[c]	
7	77.91±0.36[a]	7.67±0.18[d]	6.98±0.21[d]	21.02±0.45[f]	
9	76.82±0.54[b]	7.57±0.27[d]	6.51±0.17[e]	21.82±0.63[e]	
11	76.19±0.02[c]	7.14±0.02[e]	6.77±0.01[d]	22.3±0.02[e]	
12	70.85±0.13[g]	-7.59±0.15[f]	27.52±0.23[b]	37.49±0.23[b]	
13	72.56±0.03[e]	7.43±0.02[d]	56.64±0.07[a]	61.04±0.05[a]	

[a] pH-responsive color-change test. The pH-responsive behavior of the films was evaluated by immersing samples in standard buffer solutions covering a wide pH range. After equilibration, the films were removed and their surface color parameters were measured with a colorimeter. [b–e] Colorimetric parameters. The chromatic transition was characterized via the CIE $L^* a^* b^*$ system. L^* indicates lightness, ranging from 0 (black) to 100 (white). a^* represents the red-green axis ($+a^*$: red; $-a^*$: green). b^* represents the yellow–blue axis ($+b^*$: yellow; $-b^*$: blue). ΔE (total color difference) is calculated to quantitatively assess the overall color shift relative to a reference state. [f] Representative photographs of CMpA films after exposure to buffer solutions with different pH values, showing the pH-responsive color transition of the anthocyanin-containing film. Images were recorded under identical lighting and imaging conditions. Data are presented as mean±s.d. (n=3 spatial measurements at different positions on the same specimen).

nature portfolio

Corresponding author(s): Prof. Shangxian Xie

Last updated by author(s): Aug 28, 2026

Reporting Summary

Nature Portfolio wishes to improve the reproducibility of the work that we publish. This form provides structure for consistency and transparency in reporting. For further information on Nature Portfolio policies, see our Editorial Policies and the Editorial Policy Checklist.

Statistics

For all statistical analyses, confirm that the following items are present in the figure legend, table legend, main text, or Methods section.

n/a	Confirmed
☐	☒ The exact sample size (*n*) for each experimental group/condition, given as a discrete number and unit of measurement
☐	☒ A statement on whether measurements were taken from distinct samples or whether the same sample was measured repeatedly
☐	☒ The statistical test(s) used AND whether they are one- or two-sided *Only common tests should be described solely by name; describe more complex techniques in the Methods section.*
☒	☐ A description of all covariates tested
☐	☒ A description of any assumptions or corrections, such as tests of normality and adjustment for multiple comparisons
☐	☒ A full description of the statistical parameters including central tendency (e.g. means) or other basic estimates (e.g. regression coefficient) AND variation (e.g. standard deviation) or associated estimates of uncertainty (e.g. confidence intervals)
☐	☒ For null hypothesis testing, the test statistic (e.g. *F*, *t*, *r*) with confidence intervals, effect sizes, degrees of freedom and *P* value noted *Give P values as exact values whenever suitable.*
☒	☐ For Bayesian analysis, information on the choice of priors and Markov chain Monte Carlo settings
☒	☐ For hierarchical and complex designs, identification of the appropriate level for tests and full reporting of outcomes
☒	☐ Estimates of effect sizes (e.g. Cohen's *d*, Pearson's *r*), indicating how they were calculated

Our web collection on statistics for biologists contains articles on many of the points above.

Software and code

Policy information about availability of computer code

Data collection	Experimental data were acquired using commercial instrument-integrated software, with the corresponding instruments and acquisition procedures described in the Methods and Supplementary Information. No custom code was used for experimental data collection.
Data analysis	OriginPro 2026 (OriginLab); ImageJ v1.54p; COMSOL Multiphysics 6.2 (COMSOL AB); GROMACS 2018; Materials Studio 20.1 (BIOVIA); IBM SPSS Statistics 26. Custom Python code used for RVE generation (version 1.0.0) is publicly available without access restrictions via Zenodo at https://doi.org/10.5281/zenodo.22152551.

For manuscripts utilizing custom algorithms or software that are central to the research but not yet described in published literature, software must be made available to editors and reviewers. We strongly encourage code deposition in a community repository (e.g. GitHub). See the Nature Portfolio guidelines for submitting code & software for further information.

Data

Policy information about availability of data

All manuscripts must include a data availability statement. This statement should provide the following information, where applicable:

- Accession codes, unique identifiers, or web links for publicly available datasets
- A description of any restrictions on data availability
- For clinical datasets or third party data, please ensure that the statement adheres to our policy

All data supporting the findings of this study are available within the Article and its Supplementary Information. Source data are provided with this paper.

Research involving human participants, their data, or biological material

Policy information about studies with human participants or human data. See also policy information about sex, gender (identity/presentation), and sexual orientation and race, ethnicity and racism.

Reporting on sex and gender	n/a
Reporting on race, ethnicity, or other socially relevant groupings	n/a
Population characteristics	n/a
Recruitment	n/a
Ethics oversight	n/a

Note that full information on the approval of the study protocol must also be provided in the manuscript.

Field-specific reporting

Please select the one below that is the best fit for your research. If you are not sure, read the appropriate sections before making your selection.

☒ Life sciences ☐ Behavioural & social sciences ☐ Ecological, evolutionary & environmental sciences

For a reference copy of the document with all sections, see nature.com/documents/nr-reporting-summary-flat.pdf

Life sciences study design

All studies must disclose on these points even when the disclosure is negative.

Sample size	No statistical method was used to predetermine sample size. Experimental sample sizes were selected based on established practice for quantitative materials characterization and reproducibility assessment. Exact n values and replicate definitions are provided in the corresponding figure legends. Computational analyses used multiple initial configurations and/or RVE sections for robustness assessment rather than as experimental replicates.
Data exclusions	No data were excluded from the analysis.
Replication	Experimental measurements were repeated according to the replicate structure specified in the corresponding figure legends, with exact n values and replicate types explicitly defined. Computational robustness was evaluated using multiple MD initial configurations and multiple RVE sections/configurations as described in the Methods and Supplementary Information.
Randomization	Strawberries and fish fillets were randomly allocated to treatment groups in the preservation experiments.
Blinding	Blinding was not applied. Experimenters were only responsible for routine laboratory procedures, with all measurements performed by laboratory instruments.

Reporting for specific materials, systems and methods

We require information from authors about some types of materials, experimental systems and methods used in many studies. Here, indicate whether each material, system or method listed is relevant to your study. If you are not sure if a list item applies to your research, read the appropriate section before selecting a response.

Materials & experimental systems

n/a	Involved in the study
☒	☐ Antibodies
☒	☐ Eukaryotic cell lines
☒	☐ Palaeontology and archaeology
☒	☐ Animals and other organisms
☒	☐ Clinical data
☒	☐ Dual use research of concern
☒	☐ Plants

Methods

n/a	Involved in the study
☒	☐ ChIP-seq
☒	☐ Flow cytometry
☒	☐ MRI-based neuroimaging

Plants

Seed stocks	n/a
Novel plant genotypes	n/a
Authentication	n/a